ARTICLE IN PRESS

Available online at www.sciencedirect.com

SCIENCE DIRECT

ELSEVIER

NDT&E International ▮ (▮▮▮▮) ▮▮▮–▮▮▮

NDT&E international

www.elsevier.com/locate/ndteint

Beam-hardening in simulated X-ray tomography

K. Ramakrishna, K. Muralidhar, P. Munshi*

Nuclear & Mechanical Engineering, Indian Institute of Technology, Kanpur 208016, India

Received 31 March 2004; received in revised form 29 July 2005; accepted 19 January 2006

Abstract

Polychromatic X-ray sources are used universally in computerized tomography to obtain adequate intensity of photons. These sources, however, can produce some artifacts in the reconstructed image due to non-linearity. Beam-hardening is one such artifact, which produces false line integrals due the photon-energy dependence of the attenuation co-efficient.

The present investigation deals with the process of estimating the equivalent monoenergetic data, m, from the total attenuation, p, representing the polyenergetic X-ray beam. Three different specimens are studied which have different geometries.

Simulation results show the effect of beam-hardening and its removal (to a reasonable extent) using polynomial approximation method recommended by Herman [J Comput Assist Tomograph 1979;3:373]. The results indicate that the algorithm, proposed originally for medical application applications, is giving encouraging results for non-medical objects though the physical situations are vastly different. Future work with experimental data for non-medical objects is recommended.

Keywords: Tomography; X-ray; Beam-hardening

1. Introduction

The technique of computerized tomography (CT) has established itself as a leading tool in diagnostic radiology over the past 30 years and is catching on fast in non-destructive evaluation in a variety of situations. In the past, CT was done by X-rays only, but now other source such as γ-ray, laser and ultrasonic are also used. There has been a great deal of activity in recent years to find algorithms, that are fast when implemented on a computer and which produce acceptable reconstructions in spite of the finite and inaccurate nature of the data [1].

The measurements in computed tomography can only be used to estimate the line integrals of the absorption co-efficient of photons. Inaccuracies in these estimates are due to the width of the X-ray beam, hardening of the beam, photon statistics, etc. Radon's inversion formula is sensitive to these inaccuracies [2].

When an X-ray beam passes through the material, its attenuation at any point depends on the material at that point and on the energy distribution (spectrum) of the beam. A difficulty arises due to the fact that the X-ray beam used in computed tomography consists of photons at different energies. The attenuation at a fixed point is generally greater for photons of lower energy and the energy distribution (spectrum) of the X-ray beam changes (hardens) as it passes through the material. X-ray beam reaching a particular point inside the material from different directions are likely to have different spectra (having passed through different materials before reaching the point of interest) and thus will be attenuated differently at that point. This makes it difficult to assign a single value for the attenuation coefficient at that point inside the material.

1.1. The problem of beam-hardening

The aim of computed tomography is to obtain information regarding the nature of material occupying exact positions inside the object. In computed tomography we have two sets of measurements:

(i) calibration measurements, on which we can base an estimate of what the detector measurements would be if

*Corresponding author.
E-mail address: pmunshi@iitk.ac.in (P. Munshi).

0963-8695/$ - see front matter © 2006 Elsevier Ltd. All rights reserved.
doi:10.1016/j.ndteint.2006.01.006

the object to be reconstructed is not between the source and the detector; and

(ii) actual detector measurements with the object of interest in position.

The region, referred to as reconstruction region, is occupied by some homogeneous reference material, (such as air or water) during the calibration measurement). During the actual measurement, the object of interest is inserted into the reconstruction region, (partially) replacing the reference material. It is an important restriction that the object of interest does not occupy any point outside the reconstruction region.

Suppose that we have a monoenergetic X-ray source with photon energy $\bar{e}$. For a fixed source and detector pair, let C_m be the calibration measurement, and let A_m be the actual measurement. We can define monochromatic ray sum, m, for this beam by

$$m = -\ln\left(\frac{A_m}{C_m}\right) \tag{1}$$

and we refer to the set of m's for all source and detector pair positions as the monochromatic projection data. In practice, the X-ray beam is polychromatic. Let C_p and A_p denote calibration and the actual measurement, respectively. We can define polychromatic ray sum, p, for this beam by

$$p = -\ln\left(\frac{A_p}{C_p}\right). \tag{2}$$

We refer to the set p's for all source–detector pair positions as the polychromatic projection data.

The problem of beam-hardening is that for any source and detector pair we can obtain p, but reconstruction procedure requires m as per Eq. (1). Beam-hardening results in false gradients of the linear attenuation coefficients in the CT cross section images, indicating a non-existent density or composition gradient in the imaged object. Correction for beam-hardening effect is a must for interpreting CT images. For a given total attenuation of polyenergetic X-ray beams through the object, one has to estimate the total attenuation of monoenergetic X-ray beams through the same parts of the object which are precise enough for useful reconstruction of the monoenergetic linear attenuation coefficients in the material object. The mathematical and computational procedures in CT imaging are summarized in Fig. 1.

2. Theoretical formulation

In this section, the computational and mathematical procedures underlying the data collection, image reconstruction, formula for polyenergetic radiation and image display used in the CT are discussed.

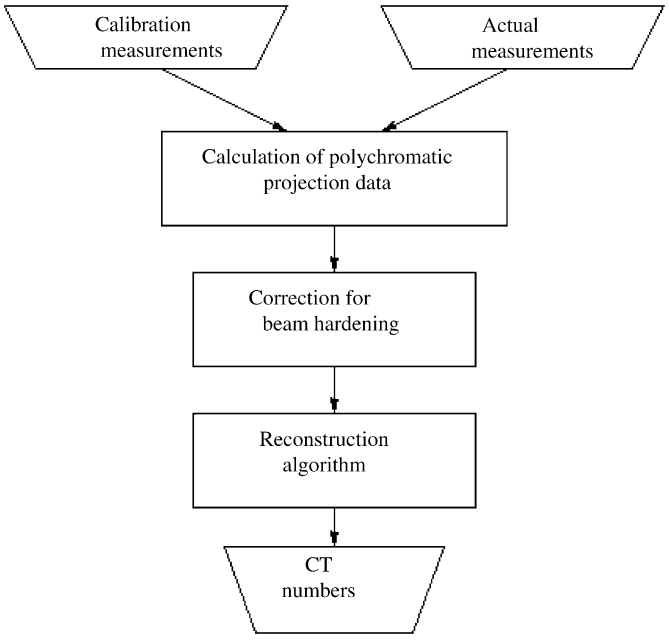

Fig. 1. Outline of the mathematical and computational procedures in CT.

2.1. Preliminaries

The number of counts of photon after passing through a curve 'c' in the material being tested is given by

$$N = N_0 \exp\left(-\int_C \mu(r,\phi)\,\mathrm{d}l\right), \tag{3}$$

where the integration is along the chord length of 'c', N is the number of photon counts after traversing the chord length, N_0 is the initial photon counts and μ is the attenuation coefficient. Since μ depends on the material and the energy of the radiation, a distribution of μ is a direct indicator of the material composition of the component being studied.

Eq. (3) can be written as

$$\ln\left(\frac{N}{N_0}\right) = \int_C \mu(r,\phi)\,\mathrm{d}l = p(s,\theta), \tag{4}$$

where $p(s,\theta)$ is called the projection data for the tomographic algorithm, and it is the integral of the function along the line specified by s and θ (Fig. 2).

The aim of tomography is to reconstruct the function $\mu(r,\phi)$, if a set of several p-values ($p(s,\theta)$) measured along various chords (c) is given. This is the fundamental problem of CT and CBP has been used in the present study for that purpose. The μ values can be suitably normalized to get the material density distribution, if so desired.

2.2. Data collection mode

The image processing methodology requires attenuation data to be collected by an array of radiation detectors for the reconstruction of the function $\mu(r,\phi)$. In this study the

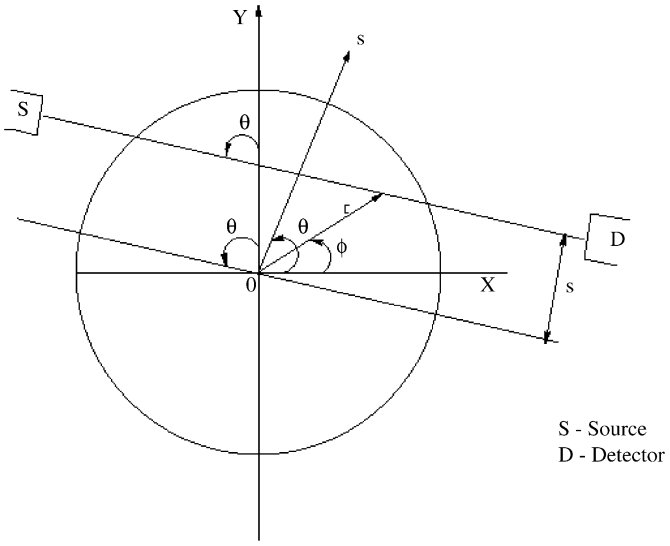

Fig. 2. Parallel-beam data collection geometry.

mode of collection is the parallel beam geometry (PBG) mode (Fig. 2). This system consists of several pairs of radiation source and radiation detector, which can scan the object completely. The SD (source detector) pairs are spaced uniformly and the object can be rotated to get the data for different views. The line SD represents the path of the data ray or the chord along which the function $p(s,\theta)$ can be found out. The perpendicular distance from the center of the object to the path of the ray is denoted by s. The object table is rotated to get several sets of 'p' for different values of θ.

Typical values of the number of rays and the number of projections used in the present work are 100 and 100. The source–detector system is moved pixel by pixel, thus generating a grid of 100×100 over the physical region of interest.

2.3. CBP algorithm

Convolution backprojection (CBP) algorithm has been described in great detail by Herman [1]. In this section we review CBP briefly as reported earlier by Munshi [3].

Fig. 2 shows the data collection geometry for a parallel beam CT scanner. The object function, $\mu(r,\phi)$, denoted for generality by $f(r,\phi)$ in subsequent equations, is represented by a unit circle and one (of many) data rays is represented by SD. The ray indices are S and θ, where S is the perpendicular distance of the ray from the object center, and θ is the angle of the source position (or object rotation). The CT data denoted by $p(s,\theta)$ given by

$$p(s,\theta) = \int_{SD} f(r,\phi)\,\mathrm{d}z. \tag{5}$$

Here, z is the variable of integration along the chord SD. The CT machine collects the projection data $p(s,\theta)$ for many values of s and θ. The "projection slice theorem" [1,2] states the equivalence of the two-dimensional Fourier transform of $f(r,\phi)$ and the 1-dimensional Fourier transform of $p(s,\theta)$ with respect to S. Symbolically

$$\hat{p}(R,\theta) = \hat{f}(R\cos\theta, R\sin\theta), \tag{6}$$

where the symbol $\wedge$ represents the Fourier transform and R is the spatial Fourier frequency. A two-dimensional Fourier inversion of Eq. (6) leads to the well-known tomographic inversion formula

$$f(r,\phi) = \int_0^{\pi}\int_{-\infty}^{\infty} \hat{p}(R,\theta)\mathrm{e}^{\mathrm{i}2\pi Rr\cos(\theta-\phi)}|R|\,\mathrm{d}R\,\mathrm{d}\theta, \tag{7}$$

where

$$\hat{p}(R,\theta) = \int_{-\infty}^{\infty} \hat{p}(s,\theta)\mathrm{e}^{-\mathrm{i}2\pi Rs}\,\mathrm{d}s. \tag{8}$$

We note that the inner integral in Eq. (7) is divergent. A practical implementation of Eq. (7) incorporates the replacement of the factor $|R|$ by $|R|W(R)$. Here $W(R)$ is a suitable window function that vanishes outside the interval $[-R_c, R_c]$ and $|R_c|$ is the Fourier cutoff frequency. Normally, $W(R)$ is an even function of R. Thus Eq. (7) takes the approximate form

$$\tilde{f}(r,\phi) \approx \int_0^{\pi}\int_{-\infty}^{\infty} \hat{p}(R,\theta)\mathrm{e}^{\mathrm{i}2\pi Rr\cos(\theta-\phi)}|R|W(R)\,\mathrm{d}R\,\mathrm{d}\,\theta. \tag{9}$$

If $\hat{p}(R,\theta)$ also vanishes for $|R| \geqslant R_c$, then the reconstructed function, denoted by $\tilde{f}$, agrees exactly with $f(r,\phi)$ with the following window function:

$$\begin{aligned} W(R) &= 1, \quad |R| \leqslant R_c \\ &= 0, \quad |R| > R_c \end{aligned} \tag{10}$$

Eq. (10) and the convolution theorem of Fourier transforms give the reconstructed function $\tilde{f}$ as

$$\tilde{f}(r,\phi) = \int_0^{\pi}\int_{-\infty}^{\infty} p(s,\theta)q(s'-s)\,\mathrm{d}s\,\mathrm{d}\theta, \tag{11}$$

where

$$q(s) = \int_{-\infty}^{\infty} |R|W(R)\mathrm{e}^{\mathrm{i}2\pi Rs}\,\mathrm{d}R \tag{12}$$

and

$$s' = r\cos(\theta-\phi). \tag{13}$$

The index s' is the data ray passing through (r,ϕ), the point being reconstructed. The inner integral in Eq. (11) is a one-dimensional convolution and the outer integral, corresponding to the averaging operation (over θ), is termed as backprojection and hence the name convolution backprojection for this particular implementation. The CBP method is also known as the filtered backprojection algorithm because of the "filtering" of the Fourier transform of the projection data $\hat{p}$ by the window (or filter) $W(R)$ in the initial stages of the formulation given by Eq. (7). The function $q(s)$, known as the convolving function, is evaluated once and stored for the repeated use for different views (or different angles θ).

For a given point (r,ϕ), the inherent error E_1, in the CBP implementation, Eq. (11) is

$$E_1(r,\phi) = f(r,\phi) - \tilde{f}(r,\phi), \tag{14}$$

where f and $\tilde{f}$ are given by Eqs. (7) and (11), respectively. This error is strictly due to finite cut-off, R_c of the Fourier frequency and is precisely zero if the projection data happens to the band-limited and the cut-off frequency is chosen to be the highest frequency contained in $\hat{p}$. In general, to avoid aliasing artifacts, we take, $R_c = 1/(2\Delta s)$, where Δs is the spacing of the data rays [1,2].

2.4. Formula for polyenergetic radiation

We summarize briefly the results of Herman [4,5] and Herman and Trivedi [6] in this section. The linear X-ray attenuation coefficient at a point inside a cross section of the object depends on the position of the point (x,y) and on the X-ray energy e. It can be denoted as $\mu(x,y,e)$. In case of monochromatic beam it can be written as (Eq. (5)),

$$m_L = \int_L \mu(x,y,e)\,\mathrm{d}l. \tag{15}$$

In case of polychromatic beam the result will not be m_L, but rather an estimate for the more complicated integral

$$p_L = -\ln \int_0^\infty \tau(e) \exp\left(-\int_L \mu(x,y,e)\right)\mathrm{d}e, \tag{16}$$

where $\tau(e)$ is the probability that the detected photon is at energy e.

The details are given by Herman [4–6].

3. Simulation of beam-hardening effect

In this section, beam-hardening effect is illustrated for certain simulated cross sections. The X-ray spectra is taken from published literature.

3.1. Simulation of polyenergetic projection data

The formula used for simulation of polyenergetic projection data is described by Herman [4,5] in detail. We summarize it here for convenience.

It is assumed that the spectrum of the X-ray beam can be approximated by a discrete spectrum consisting of J energies $e(1), e(2), \ldots, e(J)$ and that $\tau_{e(j)}$ is the probability that a detected photon (of the X-ray beam through air between the source and the detector) is at energy $e(J)$. Here it is assumed that air is the only reference medium so, that $\mu_e^a = 0$ and the equation become simpler. Let us divide the cross section into I pixels. We try to estimate the linear attenuation coefficient in each of the I pixels. Thus Eqs. (15)–(16) are replaced by

$$m = \sum_{i=1}^{I} \mu_{\bar{e}}^i Z^i, \tag{17}$$

$$p = -\ln \sum_{j=1}^{J} \tau_{e(j)} \exp\left[-\sum_{i=1}^{I} \mu_{\bar{e}(j)}^i Z^i\right], \tag{18}$$

where Z^i denote the length of intersection with the ith pixel of the line from the center of the source to the center of the detector and $\mu_{e(j)}$ is the linear attenuation coefficient at energy e in the ith pixel. Thus simulation is done on three different types of cross sections.

3.2. Specimen details

Three specimen have been designed for this simulation study. The value of the absorption co-efficient has been chosen to mimic real situations.

Fig. 3(a) shows the first specimen (S1) consisting of three small circles maintained at the same density at each of the energies. For this specimen the X-ray spectrum of Table 1 is taken from Herman [4–6]. In the original image [Fig. 3(a)], $\mu = 0.210$ is represented as green colour and $\mu = 0.416$ is represented as red colour. After beam-hardening effect (Fig. 3(b)) maximum μ found out to be 0.4961. The images are normalized between minimum 0 and maximum 0.4961.

The second specimen (S2) is a cross section consisting of two circles, two triangles, and two rectangles [Fig. 4(a)]. The materials inside them are iron, titanium and void and the X-ray spectrum given in Table 2 is taken from Hubbell [7]. The density of void is taken as zero at all the energies. Titanium is shown in blue colour ($\mu = 0.473$), iron is in yellow colour ($\mu = 0.8653$) and void is in violet colour. The beam-hardened reconstructed image, Fig. 4(b), shows that the maximum pixel value becomes

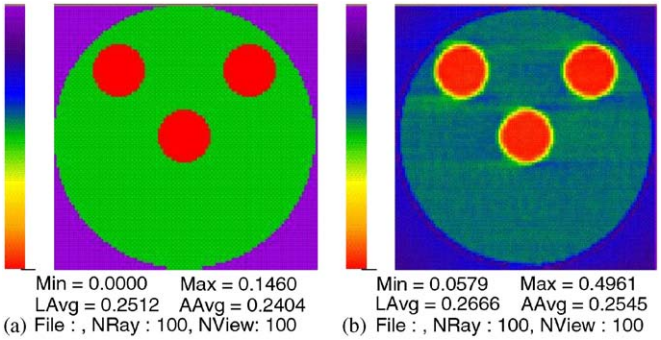

Fig. 3. Sample S1 at energy 60 keV: (a) original image; and (b) beam-hardened reconstructed image.

Table 1
X-ray spectrum for S1 [4–6]

j	$\tau_{e(j)}$	circles μ (in cm^{-1})	non-circles μ (in cm^{-1})	Energy (keV)
1	0.1	0.999	0.265	41
2	0.4	0.595	0.226	52
3	0.3	0.416	0.210	60
4	0.2	0.208	0.174	100

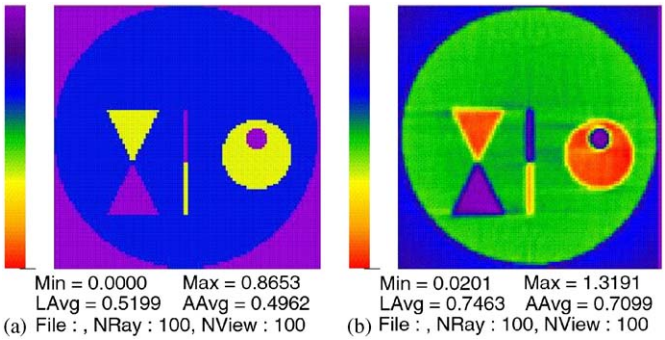

Fig. 4. Sample S2 at energy 0.3 MeV: (a) original image; and (b) beam-hardened reconstructed image.

Table 2
X-ray spectrum for S2 [7]

j	$\tau_{e(j)}$	Iron μ (in cm^{-1})	Titanium μ (in cm^{-1})	Energy (MeV)
1	0.3	2.926	1.235	0.1
2	0.4	1.1496	0.596	0.2
3	0.3	0.8653	0.473	0.3

Table 3
X- ray spectrum for S3 [4–6]

j	$\tau_{e(j)}$	star μ (in cm^{-1})	non-star area μ (in cm^{-1})	Energy (keV)
1	0.4	0.999	0.265	41
2	0.3	0.595	0.226	52
3	0.1	0.416	0.210	60
4	0.1	0.265	0.183	84
5	0.1	0.208	0.174	100

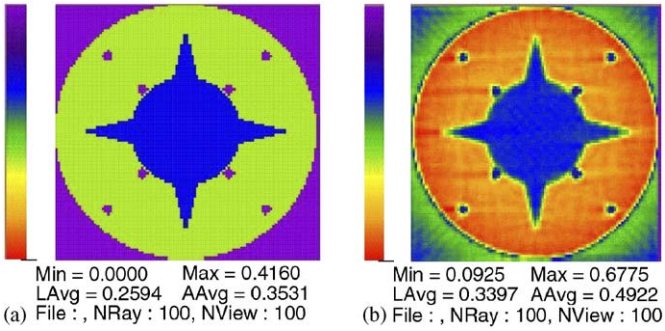

Fig. 5. Sample S3 at energy 60 keV: (a) original image; and (b) beam-hardened reconstructed image.

1.3191. The images are normalized between minimum 0 and maximum 1.3191.

Third specimen (S3) is a star-shape object whose μ values at different energies are shown in Table 3, which is taken from Herman [4–6]. There are eight small circles representing the void whose μ values are taken as zero at all the energies. These small circles have been introduced to check the contrast features of the correction algorithm. In the original image (Fig. 5(a)) the maximum pixel value is 0.416. After the beam hardening effect (Fig. 5(b)) the maximum pixel value changed to 0.6775. The linear attenuation coefficients of voids are also changed. The images are normalized between minimum 0 and maximum 0.6775.

4. Correction of beam-hardening effect

For correcting the beam-hardening effect, the procedure adopted is essentially the same as given by Herman [4–6]. It is summarized in this section.

We start with Eqs. (15)–(16) and their discretized version Eqs. (17)–(18). The least expensive type of beam-hardening correction can be done by using a function f, which is such that, for each source/detector pair, $f(p)$ is a reasonable estimate of m. Let us refer to the reconstruction from the so corrected polychromatic data $\{f(p)\}$ as the first reconstruction. It is a set of I numbers, $\mu_{\bar{e}}^{i}$, representing the estimated linear attenuation coefficient at energy $\bar{e}$ of the material in the ith of a total of I pixels.

We see that $\bar{m}$ approximates to m, and $\bar{p}$ approximates to p, and hence $f(\bar{p})$ approximates to $f(p)$. Furthermore, since the line integrals in Eqs. (15)–(16) are approximated in the same way in Eqs. (17)–(18), it appears likely that the errors, $\bar{m}-m$, and, $f(\bar{p})-f(p)$, will be similar, i.e., the difference between these errors will be considerably smaller than either of the errors). The term, $\bar{m}-f(\bar{p})+f(p)$, is an approximation to m and is superior to the use of just $f(p)$. This is true in the sense that

$$\Delta(\{f(p)+\bar{m}-f(\bar{p})\},\{m\})<\Delta(\{f(p)\},\{m\}), \tag{19}$$

where Δ represents the root mean square error. The second reconstruction is one obtained from the data $\bar{m}-f(\bar{p})+f(p)$. Since the second reconstruction is presumably more accurate than the first one, this process can be repeated. The flowchart of correction algorithm is shown Fig. 6.

5. Results

For specimen 1, Tables 4 and 5 show that average pixel error (L1 error) and RMS error (L2 error) are reduced significantly by applying this beam-hardening correction. In fact, for all the energy levels, the corrected images are very close to the monochromatic case. Also evident is the fact that the energy level of 60 keV appears to be the best for this specimen. For this energy, the match is within $\pm 0.5\%$ for both the error types. We now look at the visual input provided the corresponding CT images. Fig. 7(a) is the reconstructed image of S1 obtained by applying the first level correction. Here the third circle appears lightly. The non-circles area, green in the original image, [Fig. 7(a)] also appears very lightly. Fig. 7(b) is the second iteration as per the algorithm given in Fig. 6. All three circles appear reasonably well. It matches well with the monochromatic reconstructed image (Fig. 7(c)).

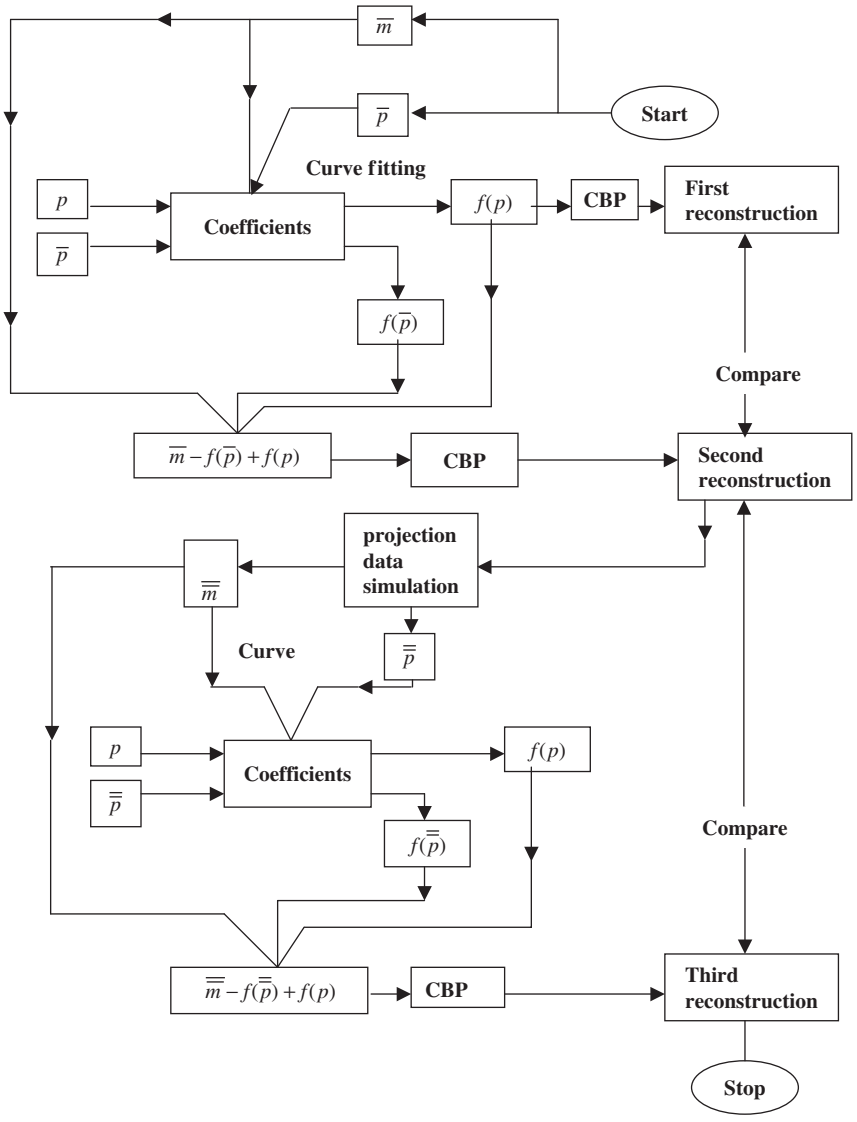

Fig. 6. Flow chart representing the correction procedure.

Table 4
Average pixel errors between the original and reconstructed images for S1

Energy (in keV)	Beam-hardening	Monochromatic	After applying correction
100	0.8026	0.0247	0.0276
60	0.0411	0.0340	0.0345
52	0.0514	0.0405	0.0411
41	0.1150	0.0558	0.0593

Table 5
Root mean square errors between the original and reconstructed images for S1

Energy (in keV)	Beam-hardening	Monochromatic	After applying correction
100	0.1052	0.0462	0.0471
60	0.0645	0.0600	0.0599
52	0.0760	0.0703	0.0705
41	0.1823	0.0977	0.1009

For specimen S2, the error details appear in Tables 6 and 7. The trend is very similar to that of specimen S1. The correction algorithm, for 0.3 MeV energy, produces images within ±0.5% of the monochromatic case. The corresponding images appear in Fig. 8.

Tables 8 and 9 show the error details for the specimen S3. Here two energy levels, 52 and 60 keV, appear to be good for this specimen. Fig. 9 shows the images for the 60 keV case. The images for the 52 keV case are similar and are not included here.

6. Discussion

Beam-hardening effect has been simulated on three simulated cross sections that mimic reality. The algorithm

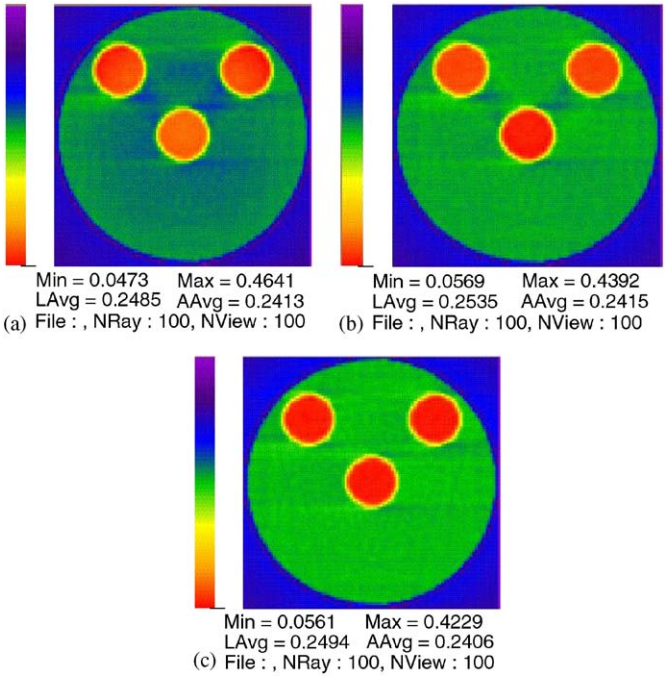

Fig. 7. Sample S1 at energy 60 keV: (a) first reconstruction; (b) second reconstruction; (c) third reconstruction; and (d) monochromatic reconstruction.

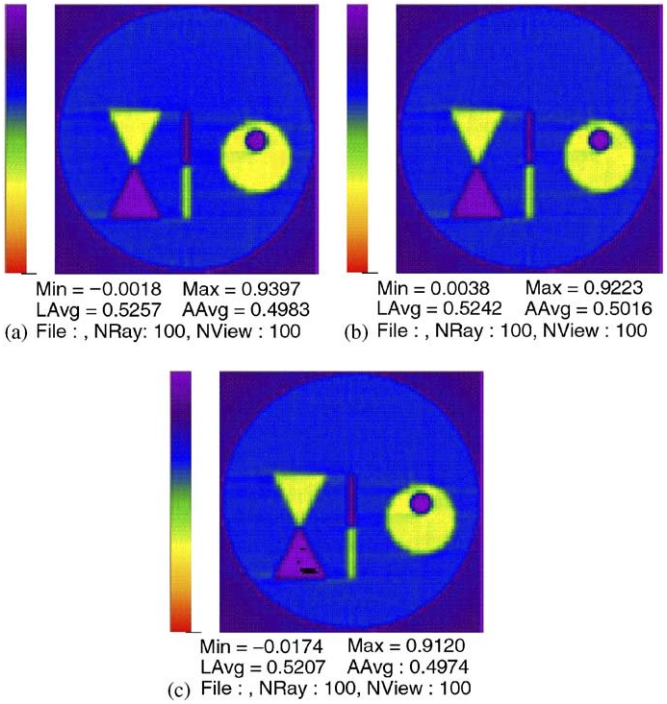

Fig. 8. Sample S2 at energy 0.3 MeV: (a) first reconstruction; (b) third reconstruction; and (c) monochromatic reconstruction.

Table 6
Average pixel errors between the original and reconstructed images for S2

Energy (in MeV)	Beam-hardening	Monochromatic	After applying correction
0.1	0.6048	0.2222	0.2244
0.2	0.1581	0.1008	0.1009
0.3	0.2477	0.0789	0.0792

Table 7
Root mean square errors between the original and reconstructed data for S2

Energy (in MeV)	Beam-hardening	Monochromatic	After applying correction
0.1	0.6970	0.3714	0.3721
0.2	0.2050	0.1705	0.1706
0.3	0.2658	0.1340	0.1342

Table 8
Average pixel errors between the original and reconstructed images for S3

Energy (in keV)	Beam-hardening	Monochromatic	After applying correction
100	0.3091	0.0309	0.0383
84	0.2735	0.0399	0.0452
60	0.1834	0.0637	0.0645
52	0.1003	0.0923	0.0930
41	0.3301	0.1569	0.1681

Table 9
Root mean square errors between the original and reconstructed images for S3

Energy (in keV)	Beam-hardening	Monochromatic	After applying correction
100	0.3314	0.0553	0.0581
84	0.2936	0.0702	0.0706
60	0.2063	0.1101	0.1089
52	0.1638	0.1577	0.1585
41	0.3650	0.2656	0.2756

chosen for correcting this effect was suggested by Herman [4–6] for medical objects. Present simulation results show that second and third order polynomials are sufficient for correcting the beam-hardening effects for non-medical objects also. The error tables and the corresponding reconstructed images show that one particular energy in the spectrum is most sensitive in bringing out the true features of the specimen. The results also indicate that two iterations are enough for correcting the beam-hardening effect. It may be mentioned here that these results, summarized by Figs. 3–9, are consistent with the Kanpur error theorems [3,8–11] and, hence, can be applied to real situations. Some edited results with experimental data are given in Appendix A.

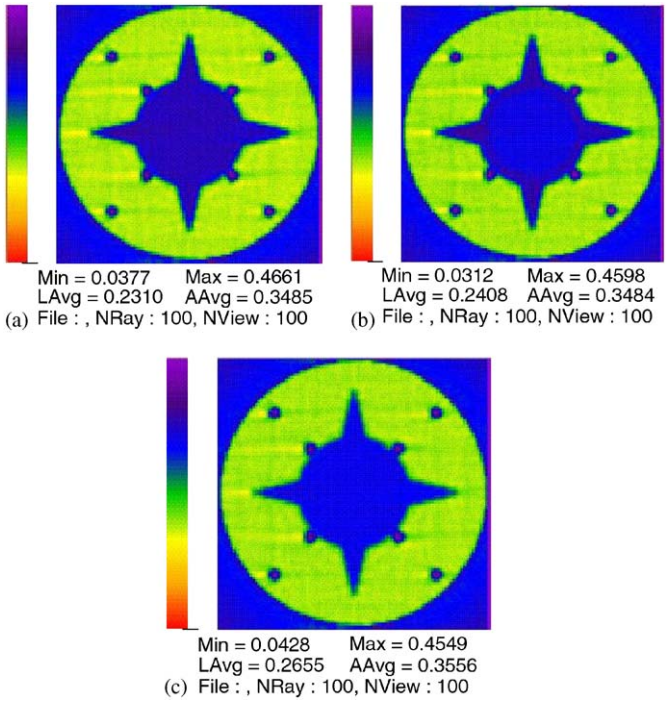

Fig. 9. Sample S3 at energy 60 keV: (a) first reconstruction; (b) second reconstruction; and (c) monochromatic reconstruction.

We may mention here that "polynomial fit" and "hardware filters" are the two existing methods to correct beam-hardening artifacts [11]. We have avoided comparison with these techniques (in this simulation exercise), as both of them are only instrument specific in nature. We are using the inherent error approach [3,7,9] to quantify the exactness of the algorithm in the work that is in progress.

Appendix A

We include here an edited version of the results that are available with us. The sample given below (Fig. A1) is an X-ray CT image of a perspex disc with five steel pins. The steel appears as yellow-red and the perspex blue and the beam-hardening artifacts show up as violet strips. The "cupping artifact" is visible clearly also on the second image on the right that is a central chord.

We now present the CT image obtained by the proposed algorithm (Fig. A2). The red coloured steel is clear with sharp circular boundary and beam-hardening artifacts are gone. Quantification of errors is done by the NMAX parameter appearing in these images.

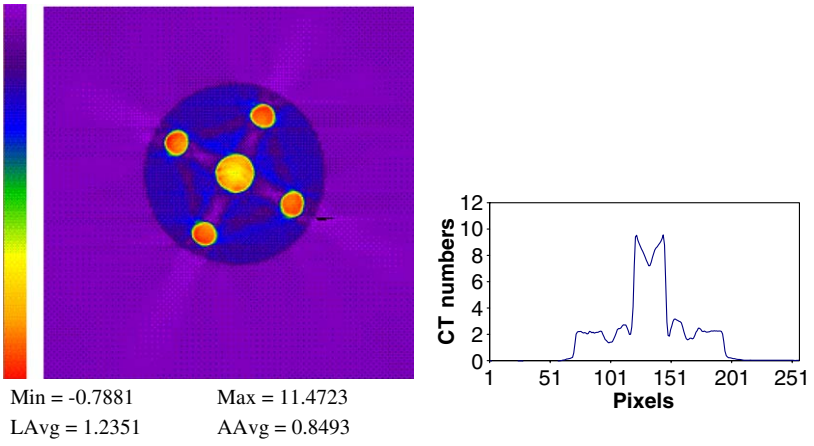

Fig. A1. Experimental results (original).

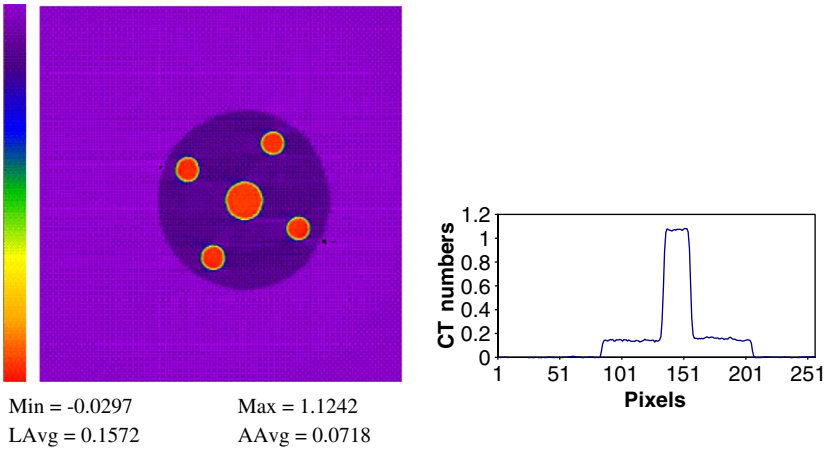

Fig. A2. Experimental results (with beam-hardening correction algorithm).

References

[1] Herman GT. Image reconstruction from projections: the mathematics of computerized tomography. New York: Academic Publishers; 1980.
[2] Natterer F. The mathematics of computerized tomography. New-York: Wiley; 1986.
[3] Munshi P. NDT E Int 1992;25:191.
[4] Herman GT. J Comput Assist Tomograph 1979;3:373.
[5] Herman GT. Phys Med Biol 1979;24:81.
[6] Herman GT, Trivedi SS. IEEE Trans Med Imaging 1983;MI-2:128.
[7] Hubbell JH. Int J Appl Radiat Ist 1982;33:1269.
[8] Munshi P, Rathore RKS, Ram KS, Kalra MS. Inverse Problems 1991;7:408.
[9] Munshi P, Maisl M, Reiter H. Mater Eval 1997;55:188.
[10] Davis G, Munshi P, Elliott JC. J X-ray Sci Technol 1996;6:63.
[11] Maisl M. Private communication. Fraunhofer Institute for Non-destructive Testing. Germany: Saarbruecken; 2005.